Effect of microstructure on the corrosion of CVD-SiC exposed to supercritical water

L. Tan [a,*], T.R. Allen [a], E. Barringer [b]

[a] Department of Engineering Physics, University of Wisconsin, Madison, Wisconsin 53706, USA
[b] Ceramic Tubular Products, Rockville, Maryland 20855, USA

ARTICLE INFO

ABSTRACT

Silicon carbide (SiC) is an important engineering material being studied for potential use in multiple nuclear energy systems including high-temperature gas-cooled reactors and water-cooled reactors. The corrosion behavior of SiC exposed to supercritical water (SCW) is critical for examining its applications in nuclear reactors. Although the hydrothermal corrosion of SiC has been the subject of many investigations, the study on the microstructural effects on the corrosion is limited. This paper presents the effect of residual strain, grain size, grain boundary types, and surface orientations on the corrosion of chemical vapor deposited (CVD) β-SiC exposed to SCW at 500 °C and 25 MPa. Weight loss occurred on all the samples due to localized corrosion. Residual strains associated with small grains showed the most significant effect on the corrosion compared to the other factors.

© 2009 Elsevier B.V. All rights reserved.

1. Introduction

The superior high-temperature mechanical properties, oxidation resistance, corrosion resistance and low neutron absorption cross-section of silicon carbide (SiC) makes it an attractive material for structural components in commercial water-cooled nuclear reactors and high-temperature Generation IV reactors. Moreover, SiC has been shown to be reasonably stable under neutron irradiation [1,2]. In recent years, SiC has been proposed for use in commercial nuclear reactors, particularly as cladding for advanced fuels, to provide substantial safety and economic benefits [3]. However, the stability of SiC in water coolants at high temperature and pressures is one of the critical performance characteristics to be demonstrated before this material can be deployed in commercial water reactors.

The corrosion behavior of SiC exposed to water has been investigated for about two decades. Oxygen content in water and the fabrication method of SiC have been found to be two important factors influencing the corrosion behavior of SiC in water. Kawakubo et al. [4] observed an increased weight loss of sintered SiC with increasing oxygen content (e.g. from <20 part-per-billion (ppb) to ~32 part-per-million (ppm) dissolved O) in pure water at 290 °C. Kim et al. [5,6] studied the effect of fabrication methods, such as reaction-bonding, sintering, and chemical vapor deposition (CVD), on the corrosion behavior of SiC exposed to pure water at 360 °C. The CVD SiC showed much higher corrosion resistance than sin-

tered and reaction-bonded SiC because of the preferential corrosion of residual free Si in the reaction-bonded SiC and at grain boundaries in sintered SiC. Preferential attack was also found at grain boundaries and around pores on the surface of sintered SiC [7]. Nagae et al. [8] observed pitting corrosion with formation of an amorphous layer (SiO_2) and intergranular corrosion due to dissolution of additives in pressureless-sintered SiC exposed to supercritical water (SCW) at 450 °C and 45 MPa for up to 50 h. Recently, pitting corrosion was also observed on CVD β-SiC exposed to deoxygenated high-purity water (<10 ppb dissolved O) at 300 °C and 10 MPa for up to 5400 h [9].

SCW refers to water with a temperature and pressure above the critical point of water at 374 °C and 22.1 MPa. It is employed in advanced water reactors to improve thermal efficiency. Because of the higher corrosion resistance compared to the other fabricated forms, CVD β-SiC has been exclusively studied for its applications in SCW reactors. Our previous study on the corrosion of a high-purity CVD β-SiC exposed to deoxygenated SCW at 500 °C and 25 MPa showed preferential attack at grain boundaries without detectable oxide scale [10]. It is believed that the corrosion of SiC in water is associated with the formation of silica and subsequent dissolution of silica into water or water vapor via the formation of soluble or volatile silicon hydroxides [9–12].

Although there are many reports about the corrosion of SiC in water, these studies mostly focused on the changes of weight, surface morphologies, and corrosion products. The effect of microstructure on the corrosion of SiC in water is limited. This paper presents the effect of residual strains, grain size, grain surface orientation, and grain boundary types on the corrosion of CVD β-SiC exposed to SCW.

---

* Corresponding author. Present address: Oak Ridge National Laboratory, One Bethel Valley Road, P.O. Box 2008 MS6151, Oak Ridge, TN 37831-6151, USA.
E-mail address: tanl@ornl.gov (L. Tan).

2. Experiment

CVD SiC samples in a size of 31.75 mm × 12.7 mm × 0.38 mm were acquired from Rohm and Hass Company. The sample geometry is further described in Ref. [10]. The samples were polished to a 1 µm surface finish followed by ultrasonic cleaning prior to exposing them to SCW for a range of exposure times at 500 °C and 25 MPa with a flow rate of ~1 m/s. To conserve time and resources, a variety of austenitic and ferritic-martensitic steels and Ni-base alloys (with a total of 28 samples) were tested simultaneously in the SCW loop at the University of Wisconsin-Madison [13]. The interaction between the samples was eliminated using alumina washers as insulators between them. The inlet oxygen content was controlled to be ~10 ppb, ~25 ppb, and ~2 ppm for each set of samples in separate tests. Deionized water with a conductivity of ~0.1 µS/cm was used for the tests. The outlet conductivity was measured to be ~0.8 µS/cm. Water chemistry analysis indicates that the outlet conductivity increase was attributed to the metallic ions released from the samples, such as Fe, Mn, and Ni (in descending order of content).

The corrosion behavior of the samples was analyzed by means of gravimetry, scanning electron microscopy (SEM), electron backscatter diffraction (EBSD), X-ray photoelectron spectroscopy (XPS), and 3-D profilometry. The samples were weighed using an electronic balance with a sensitivity of 0.1 mg before and after the SCW exposures. A LEO 1530 field-emission SEM (FESEM) was the major analytical tool employed in this study for microstructural characterization. The FESEM is equipped with EBSD capability using the TexSEM Laboratories (TSL) orientation imaging microscopy (OIM) system MSC2200. XPS for surface chemistry analysis was performed with a Perkin–Elmer PHI 5400 ESCA (electron spectroscopy chemical analysis) system. A Zygo NewView 3-D optical surface profiler was used to characterize the changes of surface topology.

3. Results and discussion

Both plan-view (PV) and cross-section (CS) of the as-received samples were polished and characterized by means of SEM and EBSD. The samples were identified as β-SiC by EBSD. The secondary electron images (SEIs), image quality (IQ), inverse-pole figures (IPFs), and strain distribution for the PV and CS surfaces are shown in Fig. 1. The SEIs show a microstructure of small equiaxed grains in the plane perpendicular to the deposition direction and large columnar grains growing along the deposition direction. The IQ images show a sharper contrast for the grain structure compared to the SEIs. The IQ, describing the quality of an EBSD pattern, is strongly affected by the perfection of the crystal lattice in the diffracting volume. Thus, lower IQ corresponds to lower contrast in the images, which is associated with distortions to the crystal lattice. The IQ images in Fig. 1 indicate that low IQ regions are primarily associated with small grains, in which more defects may exist compared to large grains. The IPF images aligned with the deposition direction of the CVD processing show the grain orientation on the PV and CS surfaces. The grains appeared to have a slight preferential (1 1 1) orientation along the deposition direction compared to the (0 0 1) and (1 0 1) orientations.

Local strains may have developed in the SiC when it was cooled down from the deposition temperature as a result of the defects and local anisotropies in the material. Local strain distribution is presented by local average misorientation between each data point and its neighbors, excluding any high-angle boundaries. The strain distribution images, as shown in Fig. 1, indicate that the strains are mainly located at regions with small grains between large grains. The intensity of the strains is classified into 9 levels in an ascending order and the area fraction for each level of strain on the PV and CS surfaces is shown in Fig. 2. The strain area fraction indicates that the CS surface has a larger strain-free area (~8%) and a smaller strained area compared to the PV surface. The larger strain-free area on the CS surface is reasonable because of the presence of large strain-free columnar grains.

The weight change of the samples exposed to the SCW with different dissolved oxygen contents is shown in Fig. 3. The limited data indicate that weight loss occurred on all the samples and the weight loss increased with increasing dissolved oxygen content in the SCW. The oxygen content effect on the corrosion of SiC is consistent with the observation at 290 °C [4]. Compared to the measured zero weight change of CVD β-SiC samples exposed to
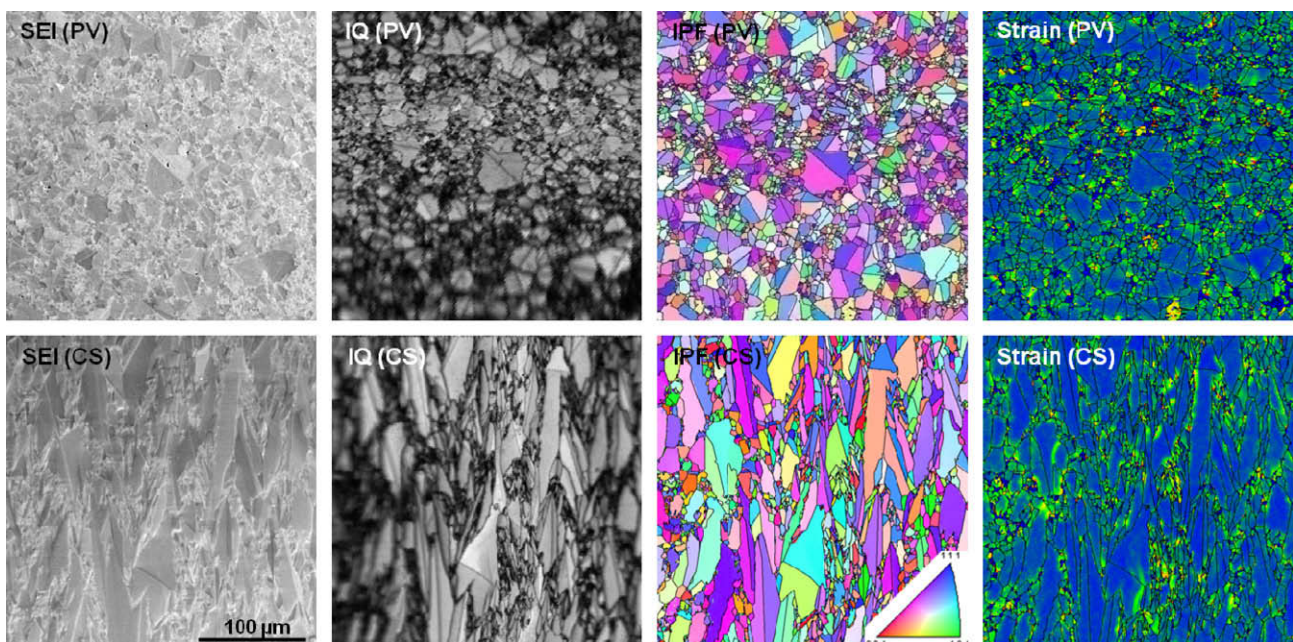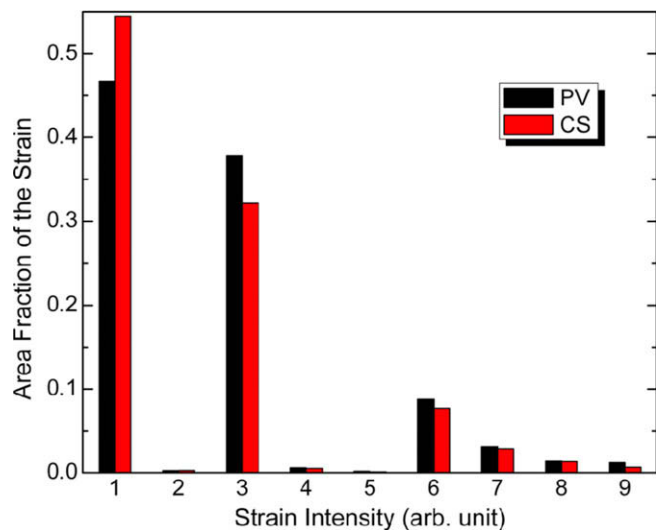

Fig. 1. Secondary electron images (SEIs), image quality (IQ), inverse-pole figures (IPFs), and strain distribution (▮▮▮ 0–5° kernel misorientation) of the as-received sample in plan-view (PV) and cross-section (CS) orientations.
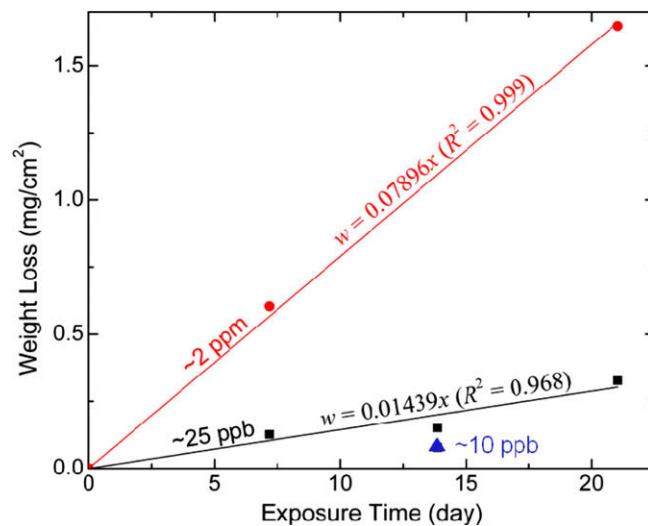
Fig. 2. Area fraction of the strains shown in Fig. 1. The strains are graded as 9 levels in an ascending sequence. Level 1 denotes strain-free region highlighted as blue and level 9 denotes the highest strain regions highlighted as red in Fig. 1. (For interpretation of the references in colour in this figure legend, the reader is referred to the web version of this article.)


Fig. 3. Weight change of the samples exposed to the SCW at 500 °C and 25 MPa with a dissolved oxygen content of ∼10 ppb, ∼25 ppb, and 2 ppm. The w, x, and R^2 are the weight loss, exposure time, and correlation coefficient, respectively.

pure water at 300 °C and 10 MPa with ∼10 ppb oxygen for up to 5400 h [9], the measurable weight loss of the sample exposed to the SCW at 500 °C and 25 MPa with ∼10 ppb oxygen (Fig. 3) is likely due to the more aggressive corrosion conditions associated with SCW. The limited data approximately followed linear corrosion kinetics for exposure time up to 505 h and dissolved oxygen contents of ∼25 ppb and ∼2 ppm. More data are necessary to determine accurate corrosion kinetics.

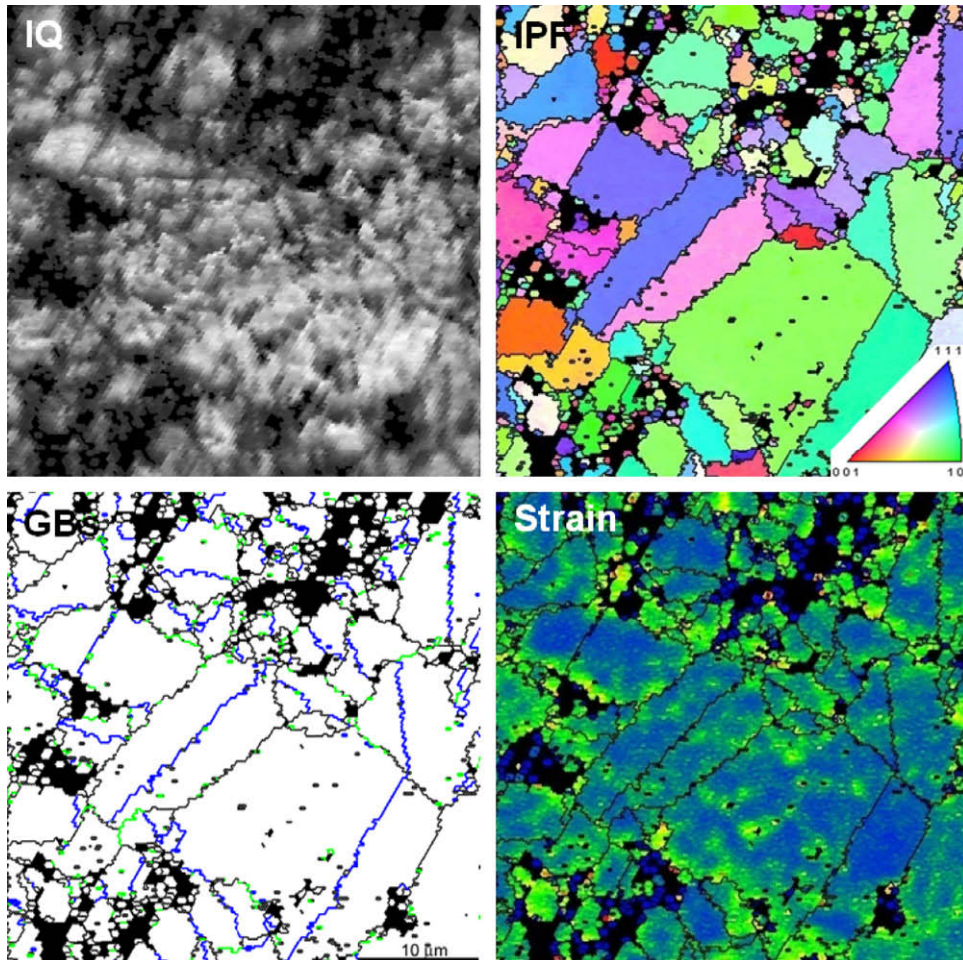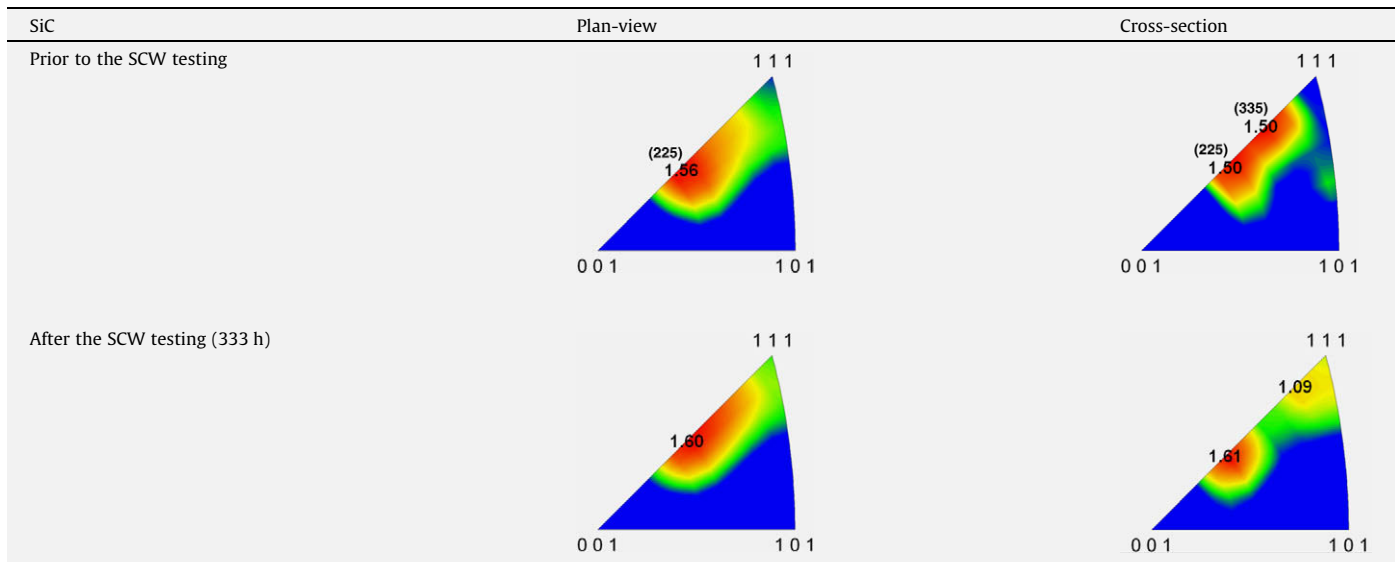The surface morphologies of the SCW-exposed samples were characterized by SEM. The typical surface morphologies of the samples in the PV and CS orientations that were exposed to the SCW with ∼10 ppb oxygen for 333 h are shown in Fig. 4. The samples exposed to the SCW with high oxygen contents and longer exposure times possess more aggressively corroded surfaces [10] and are not shown here. The PV surface shows a uniform level of corrosion across the surface. In contrast, the degree of the corrosion increased from left to right on the CS surface, as shown in Fig. 4b, which indicates a relationship existing between the amount of corrosion and the deposition/growth sequence of the CVD SiC. Unfortunately, the initial deposition side close to the substrate during CVD is not able to be identified on the samples with the available techniques.
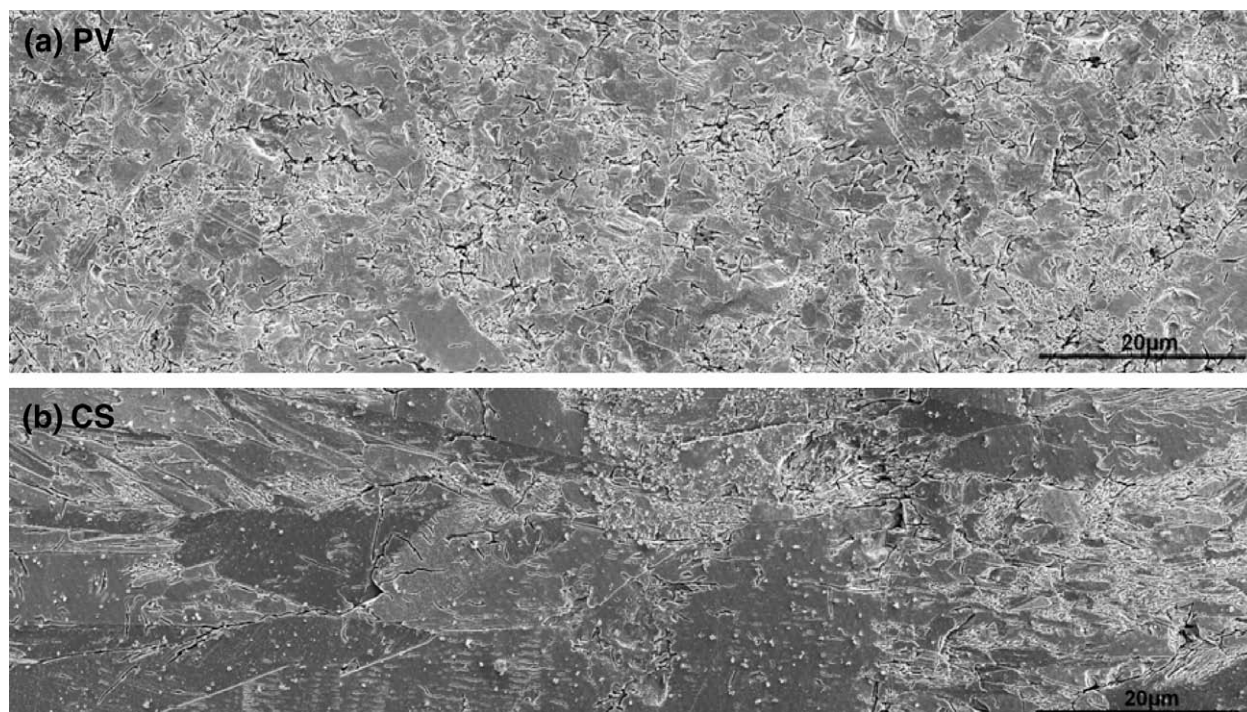
Fig. 4. Secondary electron images (SEIs) of the SCW-exposed samples (333 h, ∼10 ppb oxygen) in plan-view (PV) and cross-section (CS) orientations. The long (horizontal) side of the CS image (b) parallels the deposition direction.

Table 1
Inverse pole figures (IPFs) of the SiC sample in plan-view and cross-section orientations prior to and after the SCW testing for 333 h at 10 ppb oxygen. The IPFs are aligned with the CVD deposition direction.

SiC	Plan-view	Cross-section
Prior to the SCW testing	1 1 1 (225) 1.56 — 0 0 1 — 1 0 1	1 1 1 (335) 1.50 (225) 1.50 — 0 0 1 — 1 0 1
After the SCW testing (333 h)	1 1 1 1.60 — 0 0 1 — 1 0 1	1 1 1 1.09 1.61 — 0 0 1 — 1 0 1

Fig. 5. EBSD analysis of the plan-view surface (40 × 40 μm) of the sample exposed to the SCW with ∼10 ppb oxygen for 333 h. GBs denotes grain boundaries with blue, green, and black lines denoting $\Sigma 3$, other low-Σ CSLBs ($5 \leqslant \Sigma \leqslant 29$), and general boundaries, respectively. (For interpretation of the references in colour in this figure legend, the reader is referred to the web version of this article.)

The textures on the sample in the PV and CS orientations, as shown in Fig. 4, before and after the SCW exposure were analyzed using EBSD. The results are exhibited along with the associated inverse-pole figures (IPFs) in Table 1. The presence of a (2 2 5) texture was not changed as a result of the SCW exposure, but the intensities were slightly increased on both the PV and CS surfaces after the SCW exposure. Additionally, a distinct texture of (3 3 5) exists on the CS sample compared to that on the PV sample prior to the exposure. The measured (3 3 5) texture shifted towards (1 1 1) as compared to before the exposure.

The SCW-exposed sample surfaces in the PV and CS orientations were characterized using EBSD. Fig. 5 shows the EBSD results on the PV surface. The IQ image shows intensive defects at localized regions. Some regions are marked with black because they are not able to be identified with the EBSD. The IPF image aligned to the deposition direction does not show preferential grain orientation. The network of the grain boundaries are categorized into three groups, namely $\Sigma 3$, other low-Σ coincidence site lattice boundaries (CSLBs) ($5 \leqslant \Sigma \leqslant 29$), and general boundaries, in the GBs image. The Σ is a parameter used in the coincidence site lattice (CSL) model, and is a value defined as the reciprocal density of coincident sites at the grain boundary between two adjoining grains. By correlating the images of GBs and strain with the IQ in Fig. 5, it is deduced that corrosion primarily occurred at regions with high intensity of strains associated with small grains. Strain is expected to increase the diffusion process and dissolution kinet-

ics due to the lattice dilation introduced by the associated stress. The higher corrosion at regions with small grains may also be attributed to the large population of grain boundaries in these regions. Corrosion also occurred at grain boundaries and transgranular regions of large grains. The $\Sigma 3$ boundaries showed slightly higher corrosion resistance compared to the general boundaries.

Similar EBSD analysis was performed on the CS surface of the sample exposed to the SCW with ~10 ppb oxygen for 333 h. The analyzed region close to the left side in Fig. 4b is shown in Fig. 6. Similar to Fig. 5, the IPF image shows a variable grain orientation. The images of the GBs, strain, and IQ indicate that corrosion primarily occurred at regions with small grains associated with high strain intensity.

High-resolution secondary electron images (SEIs) for the region marked with a black square on the IQ image in Fig. 6 are shown in Fig. 7. The regions at the boundaries identified as incoherent-$\Sigma 3$ (between grains 1 and 2), $\Sigma 9$ (between grains 2 and 3), and coherent-$\Sigma 3$ (between grains 3 and 4) in Fig. 7a are magnified and shown in Fig. 7b–d, respectively. The white nano-particles on the surface may be Al_2O_3, based on the presence of an Al-2p peak in the XPS surface survey. These particles likely came from the alumina washers used for fixing the samples to the sample holder. The high-resolution SEIs show that the coherent-$\Sigma 3$ boundary is the most intact with only few nano-cracks perpendicular to the boundary. The incoherent-$\Sigma 3$ boundary was attacked at some regions, but the $\Sigma 9$ boundary was attacked almost throughout the
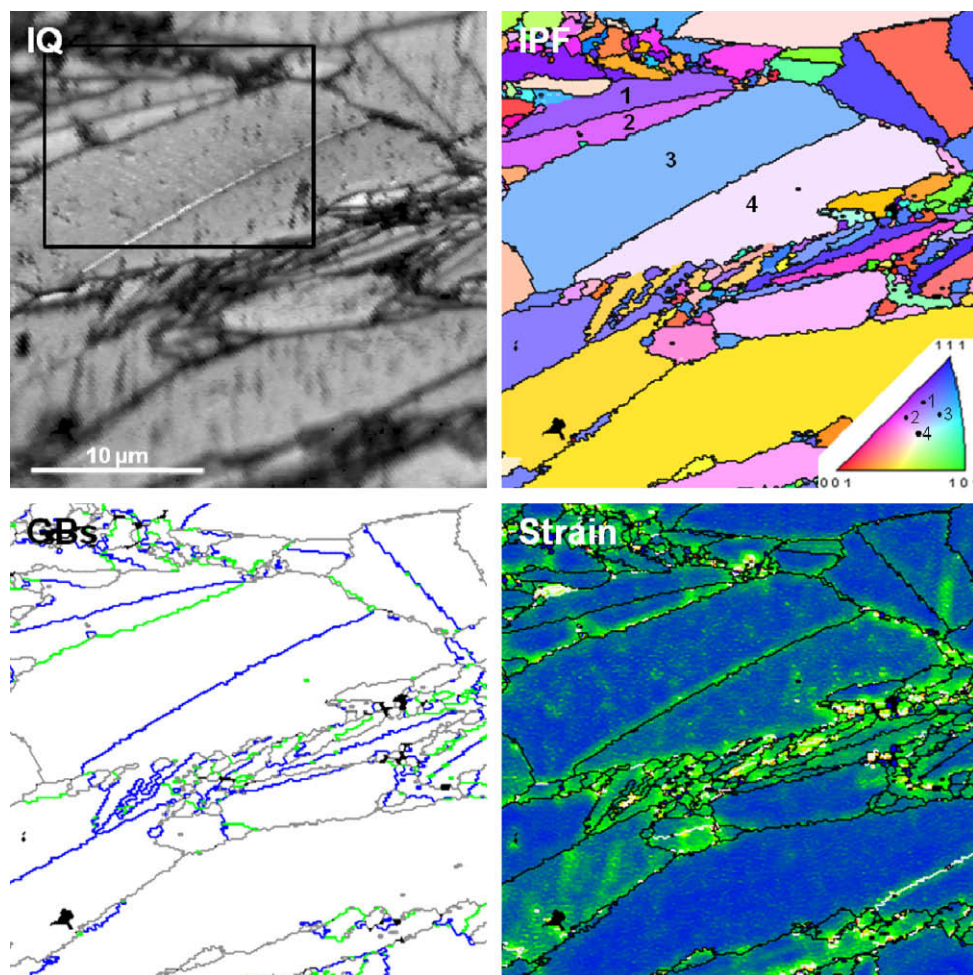
Fig. 6. EBSD analysis of the cross-section surface (28×28 μm) of the sample exposed to the SCW with ~10 ppb oxygen for 333 h. GBs denotes grain boundaries with blue, green, and gray lines denoting $\Sigma 3$, other low-Σ CSLBs ($5 \leqslant \Sigma \leqslant 29$), and general boundaries, respectively. (For interpretation of the references in colour in this figure legend, the reader is referred to the web version of this article.)
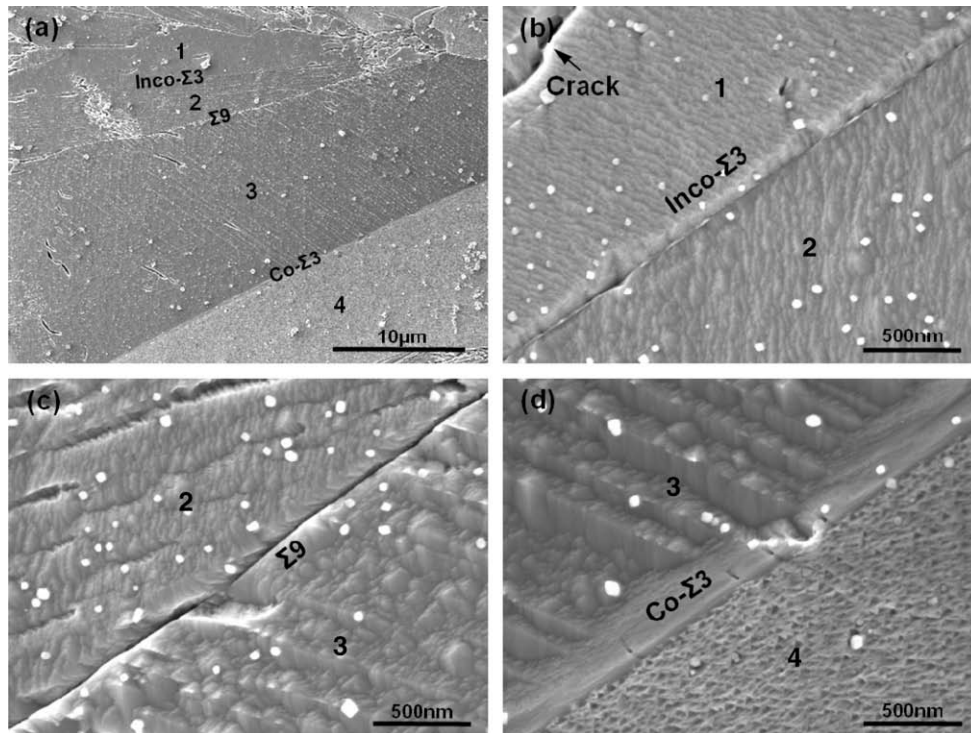
Fig. 7. Secondary electron image (SEI) of the region marked with a black square in Fig. 6. High-resolution SEIs of the regions at the incoherent-$\Sigma3$, $\Sigma9$, and coherent-$\Sigma3$ boundaries in (a) are shown in (b), (c), and (d), respectively.

boundary. The degree of attack on the three types of boundaries is consistent with the relative grain boundary energies, with the lowest energy for coherent-$\Sigma3$ boundary and the highest for $\Sigma9$ boundary [14,15].

Fig. 7 also shows different corroded morphologies for the grains 1–4. Grain 1 has a corroded morphology similar to but finer than grain 2. Grain 3 shows a sharp serrated surface close to the coherent-$\Sigma3$ boundary, which becomes dull when approaching the $\Sigma9$ boundary. Grain 4 shows dense inverted triangular pyramids. Some particles trapped in large pyramids were observed in this grain. The different corroded morphologies may be correlated with the surface orientations of the grains. As shown in the IPF image in Fig. 6, although the orientations of grains 1–4 are in the triangle zone close to the (1 1 1) plane, the deviation of these grains from the (1 1 1) plane is different. Grain 1 is closer to the (1 1 1) plane compared to the other grains. Grain 4 is close to the center of the IPF-triangle; grains 2 and 3 have similar deviation from the (1 1 1) plane, but more (0 0 1) and (1 0 1) nature, respectively. Due to the lowest surface energy (γ) of the (1 1 1) plane compared to the (1 0 1) and (0 0 1) planes of β-SiC [16], the surface energies for grains 1 through 4 may follow an ascending sequence. Surfaces with lower surface energies may have provided greater corrosion resistance, as shown in Fig. 7.

The surface roughness of the PV and CS samples exposed to the SCW testing was measured using a 3-D optical profiler. The results are listed in Table 2. Both root-mean-square (rms) and peak-to-valley (P–V) roughness values are presented. The surface roughness of the samples after the SCW exposure was greatly increased, especially for the P–V values, compared to that prior to the exposure. The greatly increased P–V roughness with large deviation indicates that localized rather than uniform corrosion is the dominant corrosion phenomena for the SiC exposed to the SCW. The rms values indicate that the roughness of the PV sample is similar to that of the CS sample prior to the testing, but it became much rougher than the CS sample after the exposure.

Table 2
Surface roughness of the plan-view and cross-section samples prior to and after the SCW exposure for 333 h. Roughness rms and P–V denote root-mean-square and peak-to-valley, respectively.

SCW	Prior to the SCW testing		After the SCW testing (333 h)	
Orientation	Plan-view	Cross-section	Plan-view	Cross-section
rms (μm)	0.037 ± 0.009	0.055 ± 0.011	0.309 ± 0.015	0.189 ± 0.013
P–V (μm)	0.505 ± 0.025	0.572 ± 0.021	9.570 ± 0.916	9.157 ± 0.898

The EBSD analyses on the PV and CS samples, as shown in Figs. 5 and 6, indicate that the corrosion occurring on the SiC was mainly induced by the localized strains at the regions associated with small grains. The analyzed area fraction of the strains as shown in Fig. 2 indicates that the PV sample had a larger area fraction of strains than the CS sample, which resulted in the rougher surface (more severe corrosion) on the PV sample. In addition to the effect of strains, corrosion also occurred at transgranular regions and grain boundaries. Low-Σ CSLBs, especially for $\Sigma3$ boundaries, showed better corrosion resistance compared to the general boundaries.

4. Conclusion

The effect of microstructure on the corrosion of CVD β-SiC exposed to supercritical water (SCW) has been analyzed by gravimetry, scanning electron microscopy, electron backscatter diffraction, and 3-D optical profilometry. Weight loss occurred on all the samples and increased with the dissolved oxygen content in the SCW. Localized corrosion occurred on both the plan-view and cross-section samples. The morphologies and roughness analyses indicate that the corrosion on the plan-view sample is more severe than that on the cross-section sample. The localized corrosion was mainly induced by the high intensity of residual

strains at regions associated with small grains. Additionally, corrosion also occurred at transgranular regions and grain boundaries. Low-Σ CSLBs, especially $\Sigma 3$ boundaries, show better corrosion resistance than the general boundaries. Grain orientations may have played a role on the different degrees of corrosion and resulting surface morphologies, and are associated with surface energies.

Acknowledgements

References

[1] E.E. Bloom, J. Nucl. Mater. 263 (1998) 7.
[2] D.J. Senor, G.E. Youngblood, C.E. Moore, D.J. Trimble, G.A. Newsome, J.J. Woods, Fusion Technol. 30 (1996) 943.
[3] D.F. Ross Jr., W.R. Hendrich, Strength testing of monolithic and duplex silicon carbide cylinders in support of use as nuclear fuel cladding, in: S. Marra, A. Wereszczak, E. Lara-Curzio (Eds.), Ceramics in Nuclear Energy Applications, A Collection of Papers Presented at the 30th International Conference on Advanced Ceramics and Composites, January 22–27, 2006, Cocoa Beach, Florida, John Wiley and Sons Inc., New Jersey, USA, 2007, pp. 117–125.
[4] T. Kawakubo, H. Hirayama, A. Goto, T. Kaneko, Zairyo 38 (1989) 300.
[5] W.J. Kim, H.S. Hwang, J.Y. Park, J. Mater. Sci. Lett. 21 (2002) 733.
[6] W.J. Kim, H.S. Hwang, J.Y. Park, W.S. Ryu, J. Mater. Sci. Lett. 22 (2003) 581.
[7] H. Hirayama, T. Kawakubo, A. Goto, T. Kaneko, J. Am. Ceram. Soc. 72 (1989) 2049.
[8] M. Nagae, T. Yoshio, K. Oda, Adv. Sci. Technol. 45 (11th International Ceramics Congress) (2006) 173.
[9] C.H. Henager Jr., A.L. Schemer-Kohrn, K.G. Pitman, D.J. Senor, K.J. Geelhood, C.L. Painter, J. Nucl. Mater. 378 (2008) 9.
[10] E. Barringer, Z. Faiztompkins, H. Feinroth, T. Allen, M. Lance, H. Meyer, L. Walker, E. Lara-Curzio, J. Am. Ceram. Soc. 90 (2007) 315.
[11] N.S. Jacobson, Y.G. Gogotsi, M. Yoshimura, J. Mater. Chem. 5 (1995) 595.
[12] G.A. Filippov, E.I. Grishanin, Yu.E. Lebedev, V.M. Trubachev, L.N. Fal'kovskii, B.I. Fonarev, Atom. Energy 102 (2007) 204.
[13] L. Tan, X. Ren, K. Sridharan, T.R. Allen, Corros. Sci. 50 (2008) 3056.
[14] V. Randle, The Role of the Coincidence Site Lattice in Grain Boundary Engineering, The Institute of Materials, Cambridge, UK, 1996.
[15] R. Skidmore, R.G. Buchheit, M.C. Juhas, Scr. Mater. 50 (2004) 873.
[16] T. Takai, T. Halicioğlu, W.A. Tiller, Surf. Sci. 164 (1985) 341.